Numerical determination of the interfacial energy and nucleation barrier of curved solid-liquid interfaces in binary systems

Julia Kundin* and Muhammad Ajmal Choudhary
Department of Engineering Science, University Bayreuth, D-95440 Bayreuth, Germany
(Received 6 April 2016; published 8 July 2016)

The phase-field crystal (PFC) technique is a widely used approach for modeling crystal growth phenomena with atomistic resolution on mesoscopic time scales. We use a two-dimensional PFC model for a binary system based on the work of Elder *et al.* [Phys. Rev. B **75**, 064107 (2007)] to study the effect of the curved, diffuse solid-liquid interface on the interfacial energy as well as the nucleation barrier. The calculation of the interfacial energy and the nucleation barrier certainly depends on the proper definition of the solid-liquid dividing surface and the corresponding nucleus size. We define the position of the sharp interface at which the interfacial energy is to be evaluated by using the concept of equimolar dividing surface (r^e) and the minimization of the interfacial energy (r^s). The comparison of the results based on both radii shows that the difference $r^e - r^s$ is always positive and has a limit for large cluster sizes which is comparable to the Tolman length. Furthermore, we found the real nucleation barrier for small cluster sizes, which is defined as a function of the radius r^s, and compared it with the classical nucleation theory. The simulation results also show that the extracted interfacial energy as function of both radii is independent of system size, and this dependence can be reasonably described by the nonclassical Tolman formula with a positive Tolman length.

DOI: 10.1103/PhysRevE.94.012801

I. INTRODUCTION

The understanding of structural and thermodynamic aspects of interfaces is important for a proper description of various applications, such as vaporization and condensation transformations, melting, and crystallization. One of the most important interfacial properties is the interfacial energy, which is a key ingredient to control the behavior of several important phenomena, such as nucleation and crystal growth. For this reason, various theoretical approaches have been developed to estimate the interfacial energy. To date, these approaches can only be viewed as estimates of the interfacial energy due to the large number of assumptions. The influence of the surface curvature and the diffuse nature of the interface on its equilibrium properties is still not fully understood due to the presence of a finite diffuse layer which gives rise to various definitions of the nucleus size as well as raises questions about the actual surface where the interfacial energy is to be evaluated [1]. In contrast to the planar interface, the surface area of the curved diffuse interface directly depends on the droplet size, and even a small change in radius results in a significant shift in the resulting interfacial energy. Bohr *et al.* reported that a small fluctuation of the order 0.5 fm in the radius of nucleus within the diffuse interface region leads to a shift of the order of 10^2 MeV in the resulting surface energy of Pb [2].

In the 1990s, several nonclassical theories of crystal nucleation were developed which explained the dependency of the interfacial energy on the undercooling and the corresponding nucleus size that contradicts the classical nucleation theory (CNT). In the context of nonclassical theories, the modified self-consistent classical theory [3,4], the field theoretic approaches based on the density functional theory [5–7], and the diffusion interface theory [8–10] were introduced (see also a recent review of nonclassical theories in [11]). Various phenomenological dependencies of the interfacial energy on the nucleus size were also proposed [4,12]. A well established nonclassical theory of the liquid-vapor phase separation was developed by Tolman [13]. It proposed that the surface tension of small liquid droplets existing in equilibrium with the vapour phase depends on its radius as

$$\gamma(r) = \frac{\gamma_\infty}{1 + \frac{2\delta_T}{r}}, \tag{1}$$

where δ_T is the Tolman length. A number of investigations based on the Gibbs dividing surface approach have been performed to study the dependence of δ_T on the temperature and radius. A recent review of that approach was done by Tröster *et al.* [13].

In contrast to the theoretical attempts, several simulation techniques provide the possibility to compute the interfacial energy more efficiently with much higher accuracy. The properties of the interface on the atomic scale were investigated in many works by means of Monte Carlo (MC) and molecular dynamics (MD) simulations [14,15]. In [14], the nonclassical nucleation barrier of a liquid-gas system is defined as a function of the supercooling $\delta\rho = \rho_1 - \rho_2$ according to the following relation:

$$\Delta F(\delta\rho) = \frac{4\pi r^3}{3}(F_1 - F_2) + 4\pi r^2 F_I, \tag{2}$$

where F_1 is the free energy of the gas at the density ρ_1, F_2 is the free energy of the gas at the density ρ_2, and F_I is the interfacial energy evaluated by MC simulations. It was shown that the nonclassical nucleation barrier differs from the classical theory at large $\delta\rho$, and this difference vanishes at a critical value. As a prolongation of this work [15], another method was developed in which the surface energy of liquid droplets was obtained from the Helmholtz free energy function in the grand canonical ensemble calculated by MC simulation. This method focuses

*julia.kundin@uni-bayreuth.de

on the equilibrium properties of the vapor-liquid coexistence region.

In addition to the MC and MD simulations, the phase-field crystal (PFC) modeling derives its attractiveness from the fact that it does not need any explicit tracking of the interface, and thus the satisfaction of complicated interfacial boundary conditions is not needed. In comparison to the traditional phase-field models, the periodic atomic density field in the PFC model can give an additional contribution to the definition of the interfacial energy and can explain various size effects observed in the MC and MD methods [16–19]. The PFC model has emerged as an efficient simulation tool for problems involving a tightly coupled atomic and continuum scale. It is a phenomenological but still quite generic approach to describe crystals of isotropic as well as anisotropic building blocks [20–23]. Thus, in the multiple time- and length-scale diagrams of materials modeling it provides a bridge between atomistic and continuum simulation techniques.

Recently, we proposed a method for the investigation of the liquid-solid interface by means of the PFC model for a binary system [24]. The main focus of this study is to demonstrate the usefulness of the finite system size approach to derive the liquid-solid interfacial energy and its dependence on the droplet (cluster) radius. It was shown that the interfacial energy for small droplets deviates from the predictions based on CNT. In [24], we defined the droplet (cluster) size by using the concept of the equimolar dividing surface. However, according to the Gibbs-Tolman concept [25,26], two different radii or dividing surfaces can be introduced. The first radius (r^e) is the equimolar radius, which corresponds to the equimolar dividing surface and defines the physical size of the droplet, i.e., the actual surface at which the surface tension is applied. The second radius (r^s) is the surface tension radius, which provides the minimum of the surface tension coefficient. In recent studies of liquid droplets [27,28], it was shown that the difference of the radii $r^e - r^s$ in an asymptotic limit of large systems derives the Tolman length. This means that, for the calculation of the curvature correction to the surface energy, a finite layer in the particle distribution should be taken into account. In this framework, Toth and Granasy [29] defined the surface energy, the nucleation barrier, and the Tolman length for two pure metals and a binary alloy using the equimolar radius r^e calculated by the phase field approach and the radius of the surface tension r^s defined by diffuse interface theory [10].

In the present work, we highlight further improvements in the finite size approach for the derivation of the liquid-solid interfacial energy and the nucleation barrier by comparing the simulation results based on two concepts used for the description of dividing surface (r^e and r^s). More specifically, the main goal of this article is to define a precise sharp interface at which the interfacial energy can be evaluated by using the concept of the equimolar dividing surface and the concept of the minimization of the interfacial energy as well as to extract the corresponding nucleus-size-dependent interfacial energies and nucleation barriers for both concepts. This study will also demonstrate how the definition of the dividing surface influences the resulting interfacial energy and the nucleation barrier for small nucleus sizes.

This paper is organized as follows. In Sec. II, we present the mathematical formulation of the PFC model for binary systems and calculate the equilibrium phase diagram. In Sec. III, we briefly describe the simulation scheme for the investigation of the liquid-solid interface. In Sec. IV, two methods of the evaluation of the interfacial energy are presented based on the definition of the dividing liquid-solid surface; i.e., the definition based on the minimum interfacial energy and the equimolar dividing surface. The simulation results for the calculation of the interfacial energy and nucleation barriers for various cluster sizes are presented in Sec. V. Furthermore, we present a comparison of simulation results with the predictions based on the classical as well as nonclassical theories.

II. PHASE-FIELD CRYSTAL MODEL FOR BINARY SYSTEMS

In this section, we briefly introduce the PFC model for binary systems based on the work of Elder *et al.* [17] and describe the method for the evaluation of the equilibrium phase diagram by using the common tangent construction technique.

A. Model description

We consider a binary system composed of two components A and B, with representative atomic number densities, i.e., ρ_A and ρ_B, respectively. The free energy for such a binary system includes contributions from the energy of density fields of both components and their interaction. A dimensionless atomic density field n and a dimensionless concentration field c can be written as

$$\begin{aligned} n &= \frac{\rho_A + \rho_B}{\bar{\rho}} - 1, \\ c &= \frac{\rho_B - \rho_A}{\bar{\rho}}, \end{aligned} \tag{3}$$

where $\bar{\rho}$ is the mean density of the system. We refer to these fields as diffusion fields in the following sections of this paper.

The free energy functional for a binary system is derived in the form

$$\mathcal{F} = \int F(n,c)d\vec{r}, \tag{4}$$

with the dimensionless total free energy

$$\begin{aligned} F(n,c) = \frac{n}{2}[B^l + B^s(2R^2\nabla^2 + R^4\nabla^4)]n - \frac{t}{3}n^3 + \frac{v}{4}n^4 \\ - \gamma c + \frac{w}{2}c^2 - \frac{\xi}{2}c^3 + \frac{u}{4}c^4 + \frac{\epsilon^2}{2}|\vec{\nabla}c|^2 + \cdots, \end{aligned} \tag{5}$$

where t, v, γ, w, ξ, u, and ϵ are constant model parameters. B^l, B^s, and R depend on the concentration and can be expressed by Taylor expansion. Assuming B_0^l, B_0^s, B_2^l, and R_0 to be the only nonzero coefficients for mathematical simplicity, one ends up with the following expressions:

$$\begin{aligned} B^l &= B_0^l + B_2^l c^2, \\ B^s &= B_0^s, \\ R &= R_0. \end{aligned} \tag{6}$$

The components of an alloy can have various atomic sizes. In this case, by choosing R as a concentration dependent value, the additional elastic strain will arise on the interface and lead to increasing interfacial energy.

The energy parameters in this paper are expressed in units of $\bar{\rho}k_BT$, where k_B is the Boltzmann constant and T is the temperature, and space parameters are given in units of the lattice constant a.

Considering substitutional diffusion between both components A and B, i.e., equal mobility of the components, one gets decoupled dynamical equations for both diffusion fields n and c. In a simple case, if one assumes a constant mobility (M), then the dynamical equations can be written as

$$\frac{\partial n}{\partial t} = M\nabla^2\frac{\delta\mathcal{F}}{\delta n}, \tag{7}$$

$$\frac{\partial c}{\partial t} = M\nabla^2\frac{\delta\mathcal{F}}{\delta c}. \tag{8}$$

Using the free energy expression (5), we obtain the derivative of the free energy with respect to the atomic density, i.e.,

$$\frac{\delta\mathcal{F}}{\delta n} = nB^l - tn^2 + vn^3 + \frac{B^sR^2}{2}[(2\nabla^2 + R^2\nabla^4)n] + \frac{B^s}{2}[2\nabla^2(nR^2) + \nabla^4(nR^4)] \tag{9}$$

and the derivative of the free energy with respect to the concentration field, i.e.,

$$\frac{\delta\mathcal{F}}{\delta c} = B_2^lcn^2 - \gamma + wc - \xi c^2 + uc^3 - \epsilon^2\nabla^2c. \tag{10}$$

A one-mode approximation technique is used to initialize the total density n, i.e.,

$$n = n_0 + A\left(\frac{1}{2}\cos\left[\frac{2qy}{\sqrt{3}}\right] - \cos(qx)\cos\left[\frac{qy}{\sqrt{3}}\right]\right), \tag{11}$$

where A is the amplitude and q is the wave number. Inserting this expression into (5) and then minimizing with respect to q and A gives the equilibrium values

$$q^{eq} = \frac{\sqrt{3}}{2R},$$
$$A_{\min} = \frac{4\left(t - 3vn_0 + \sqrt{t^2 + 24tvn_0 - 36v^2n_0^2 - 15v\Delta B}\right)}{15v}, \tag{12}$$

where $\Delta B = B^l - B^s = \Delta B_0 + B_2^lc^2$ with $\Delta B_0 = B_0^l - B_0^s$ being a linear function of the temperature.

B. Phase equilibrium

The binary PFC model [17] was developed for a binary alloy with two components. One component is taken as a solute and the second component is taken as a matrix. In the current scenario, it is similar to the phase-field model for binary alloys with one concentration field. However, in reality, the PFC model contains two diffusion fields, because the system has three components: A, B, and empty places. If the atomic density field decreases the densities of particles, A and B decrease too, and we have an increase in empty places. In general, the liquid and solid phases have different mean densities. Hence, to describe a three-component system, the model should have two density fields, while one component is the matrix. It is similar to ternary alloy systems, and we can state that our system can be considered a multicomponent system.

The equilibrium phase diagram for the model can be calculated using the following set of nonlinear equations:

$$\begin{aligned}
\mu_s^n\left(c_s^{eq}, n_{0,s}^{eq}\right) &= \mu_l^n\left(c_l^{eq}, n_{0,l}^{eq}\right) = \mu^{n,eq},\\
\mu_s^c\left(c_s^{eq}, n_{0,s}^{eq}\right) &= \mu_l^c\left(c_l^{eq}, n_{0,l}^{eq}\right) = \mu^{c,eq},\\
\omega_s\left(c_s^{eq}, n_{0,s}^{eq}\right) &= \omega_l\left(c_l^{eq}, n_{0,l}^{eq}\right),
\end{aligned} \tag{13}$$

where $\mu_{s/l}^n$ and $\mu_{s/l}^c$ are the diffusion potentials and $\omega_{s/l}$ are the grand potential densities of the solid and liquid phase, which are defined as

$$\omega_{s/l}\left(c_{s/l}^{eq}, n_{0,s/l}^{eq}\right) = \bar{F}_{s/l}^{eq} - \mu^{c,eq}c_{s/l}^{eq} - \mu^{n,eq}n_{0,s/l}^{eq}. \tag{14}$$

It is important to mention here that Eq. (13) is similar to the equations for a ternary alloy, which are based on the common tangent construction between the Gibbs free energies of two phases (see, e.g., Ref. [30]).

In Eq. (14), the mean solid free energy density is calculated as an integral over the system box:

$$\bar{F}_s = \frac{\sqrt{3}}{2\pi^2}\int_0^{\frac{2\pi}{\sqrt{3}}} dx \int_0^{\pi} dy\, F_s(x,y) \tag{15}$$

with

$$F_s(x,y) = B^l\frac{n^2}{2} + B^s\frac{n}{2}\left[2\left(\frac{\partial^2}{\partial x^2} + \frac{\partial^2}{\partial y^2}\right) + \frac{\partial^4}{\partial x^4} + \frac{\partial^4}{\partial y^4} + 2\frac{\partial^4}{\partial x^2\partial y^2}\right]n - \frac{tn^3}{3} + \frac{vn^4}{4} - \gamma c + \frac{wc^2}{2} - \frac{\xi c^3}{3} + \frac{uc^4}{4}. \tag{16}$$

The mean liquid free energy density is defined as

$$\bar{F}_l = F_l = B^l\frac{n_0^2}{2} - \frac{tn_0^3}{3} + \frac{vn_0^4}{4} - \gamma c + \frac{wc^2}{2} - \frac{\xi c^3}{3} + \frac{uc^4}{4}. \tag{17}$$

The corresponding diffusion potentials are defined as

$$\mu_s^n = \frac{\sqrt{3}}{2\pi^2}\int_0^{\frac{2\pi}{\sqrt{3}}} dx \int_0^{\pi} dy\frac{\partial F_s}{\partial n}, \quad \mu_s^c = \frac{\partial\bar{F}_s}{\partial c}, \quad \mu_l^n = \frac{\partial\bar{F}_l}{\partial n_0}, \quad \mu_l^c = \frac{\partial\bar{F}_l}{\partial c}. \tag{18}$$

To calculate the equilibrium parameters of the phase diagram, one first chooses a value $n_{0,l}^{eq}$ and then calculates other parameters: c_s^{eq}, $n_{0,s}^{eq}$, and c_l^{eq} corresponding to the chosen value $n_{0,l}^{eq}$ by solving Eq. (13).

For our investigations, we calculated the section of the equilibrium phase diagram at the undercooling $\Delta B_0 = 0.05$ as shown in Fig. 1. The regions of the liquid and solid phases as well as the region of the coexisting of both phases are clearly identified in the figure. The model parameters used in the calculations are listed in Table I.

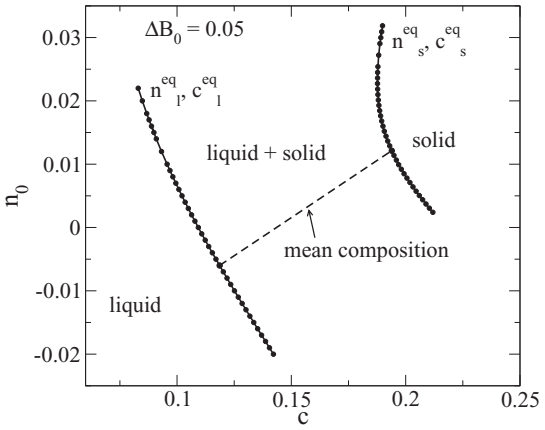

FIG. 1. Section of the equilibrium phase diagram at $\Delta B_0 = 0.05$. The region of the initial concentrations used in the following simulations is identified by a broken line.

III. SIMULATION SCHEME FOR THE INVESTIGATION OF THE LIQUID-SOLID INTERFACE

Simulations are performed for two cases, i.e., a circular solid cluster surrounded by the liquid phase. The governing model equations (7) and (8) are solved numerically in two- dimensions on a system domain of size $L_x \times L_y$ with $L_x = La$, $L_y = La\sqrt{3}/2$. The corresponding area of the simulation box is $A = L^2a^2\sqrt{3}/2$. One unit cell has a size $a \times \sqrt{3}/2a$. Note that the lattice constant is defined as $a = 2\pi/q^{eq} = 4\pi R/\sqrt{3} \approx 7.26$. The discretization size is chosen $\Delta x = \Delta y = a/9 \approx 0.806$. The number of the discretization points is calculated as integer values $N_x = (\text{int})L_x/\Delta x$, $N_y = (\text{int})L_y/\Delta y$. In one unit cell we have around $9 \times 9\sqrt{3}/2 \approx 9 \times 8$ discretization points.

We initialize simulations with a sufficiently small time step of $\Delta t = 0.0005$ to ensure the stability of the scheme. The result of test simulations showed that after 150 000 steps the resulting system parameters change very slowly. Based on these findings, we changed the time step to $\Delta t = 0.0015$ after 400 000 steps.

For the simulation the simple explicit Euler method was used for the time discretization and the spherical Laplacian approximation was used for the space derivatives [17]. Periodic boundary conditions are applied in all directions of the domain. The periodic boundary condition in the y direction is not perfect due to the choice of Δy. To avoid the influence of the boundaries, we limit the nucleus size using small phase fractions. The initial solid cluster was inserted in the center of the simulation box. In order to investigate the influence of system size on final results, we varied the size of the simulation box, i.e., $L = 30,40,\ldots,80$. The initial phase fractions are varied as $p_s^{\text{in}} = 0.25,0.2,0.15,0.1$. The radius of an initial solid cluster (r^{in}) is defined as a function of the initial solid phase fraction, i.e.,

$$r^{\text{in}} = \left(\frac{p_s^{\text{in}} A}{\pi}\right)^{1/2}. \tag{19}$$

To ensure the conservation law we used $p_s^{\text{in}} + p_l^{\text{in}} = 1$.

The initial values for the diffusion fields are chosen as equilibrium values for the liquid phase and for the solid phase [n is initialized by Eq. (11) with $A_{\min}$ and q^{eq}]. The initial parameters used in the simulations are listed in Table II. They slightly differ from the equilibrium parameters in the phase diagram to take into account the change of the equilibrium concentrations near the curved interface according to the Gibbs-Thomson effect.

The average values of the diffusion fields $\bar{c}$ and $\bar{n}$ are defined by the initial phase fractions, i.e.,

$$\begin{aligned} \bar{c} &= c_s^{\text{in}} p_s^{\text{in}} + c_l^{\text{in}}\left(1 - p_s^{\text{in}}\right), \\ \bar{n} &= n_s^{\text{in}} p_s^{\text{in}} + n_l^{\text{in}}\left(1 - p_s^{\text{in}}\right). \end{aligned} \tag{20}$$

The average values of the diffusion fields $\bar{c}$ and $\bar{n}$ should be constant during one simulation run.

In these investigations, we calculate the following parameters after each simulation run: the mean free energy density of the system ($\bar{F}$), the mean diffusion potentials of the system ($\mu^{n/c}$), free energy densities and diffusion potentials in each phase ($F_{s/l}$, $\mu_{s/l}^{n/c}$), the mean diffusion fields of the system, and the diffusion fields in each phase ($\bar{c}$, $\bar{n}$, $c_{s/l}$, $n_{s/l}$). These

TABLE I. Model parameters used in simulations.

B_0^l	B_0^s	B_2^s	R_0	t	v
1.05	1.0	−1.663	1.0	0.6	1.0
γ	w	ξ	u	ϵ	
0.002	0.088	0.59	4.0	1.2	

TABLE II. The parameters used in the simulation as initial values, the diffusion potentials, and the corresponding equilibrium values from the phase diagram.

	Parameter					
	$n_{0,s}$	$n_{0,l}$	c_s	c_l	μ_s^n	μ_s^c
Initial	0.01380	−0.0088	0.2090	0.1000	−0.009171	0.00477
Equil.	0.01347	−0.0063	0.1925	0.1169	−0.006484	0.00460

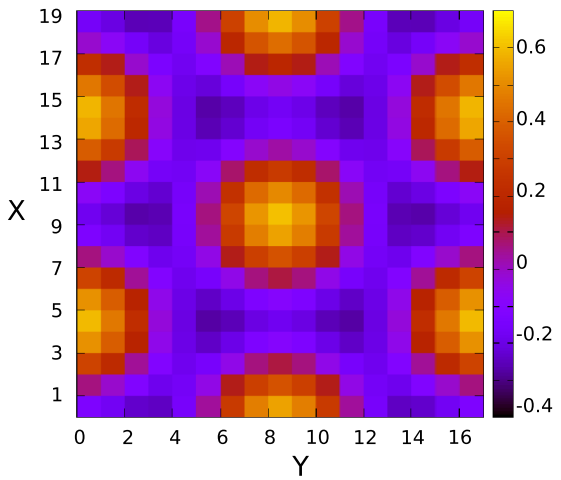

FIG. 2. Four unit cells in the center of the simulation box used for the calculation of averaging parameters in the solid phase.

quantities, corresponding to different phases, are calculated by averaging in four unit cells, which are lying in the center of the box for the solid phase and on the left bottom corner of the box for the liquid phase. The area of averaging for the solid phase is shown in Fig. 2. The simulations keep running until the system achieves the desired equilibrium state, i.e., when the values of diffusion potentials in both phases are equal up to nine digits. The final coexistence values for each phase ($c_{s/l}$, $n_{s/l}$, $F_{s/l}$), the mean free energy density ($\bar{F}$), and the mean diffusion potentials of the system ($\mu^{n/c}$) in the coexistence are used for the calculation of the interfacial energy in Sec. V.

IV. THEORETICAL DEFINITION OF THE INTERFACIAL ENERGY

In this section, we present a detailed description of the two concepts that we used to define the position of the dividing surface for a solid-liquid phase coexistence and the extraction of the corresponding interfacial energy.

A. Definition of the minimum interfacial energy

In this subsection, we derive the dividing surface for a system with an arbitrary number of diffusion fields for the case of solid-liquid coexistence by using the concept of the minimum interfacial energy for the definition of a droplet radius [27,31]. We consider a system of size V in three-dimensional space, which contains a solid cluster of volume $V_s = 4\pi r^3/3$ with the surface area $S = 4\pi r^2$ in the liquid matrix of volume $V_l = V - V_s$. The solid phase fraction is calculated as $p_s = V_s/V$. We define ν number of diffusion fields in this derivation. The values of diffusion fields in the solid and liquid phases are identified as $\rho^i_{s/l}$, where i is the index for a field. For our binary PFC model, we have two diffusion fields n and c.

The free energy of the system can be written as a sum of the volume and surface contributions

$$\mathcal{F} = \mathcal{F}_V + \mathcal{F}_S, \tag{21}$$

where

$$\mathcal{F}_V = \omega_s V_s + \omega_l V_l + \sum_i^{\nu} \mu^i \left(\rho^i_s V_s + \rho^i_l V_l\right) \tag{22}$$

and

$$\mathcal{F}_S = \gamma S + \sum_i^{\nu} \mu^i \rho^i_I S. \tag{23}$$

Here $\omega_{s/l} = F_{s/l} - \sum_i^{\nu} \mu^i \rho^i_{s/l}$ are the grand potential densities in the liquid and solid phase, γ is the interfacial energy, and ρ^i_I are the excess diffusion fields at the interface. One can define the mean diffusion fields in the system, $\bar{\rho}^i$, as

$$\bar{\rho}^i = \rho^i_s V_s/V + \rho^i_l V_l/V + \rho^i_I S/V. \tag{24}$$

From Eqs. (21)–(24), one can get an expression for γ as

$$\gamma = \frac{\mathcal{F} - \sum_i \mu^i \bar{\rho}^i V - (\omega_s V_s + \omega_l V_l)}{S}. \tag{25}$$

We define $\Omega = \mathcal{F} - \sum_i \mu^i \bar{\rho}^i V$ as the mean grand potential of the system and $\omega = \Omega/V = \bar{F} - \sum_i \mu^i \bar{\rho}^i$ as the mean grand potential density of the system with $\bar{F} = \mathcal{F}/V$. Equation (25) can be transformed to Eqs. (26) and (27) by adding the term $-\omega_l V_s + \omega_l V_l$, i.e.,

$$(\omega - \omega_l)V = -\Delta\omega_{ls} V_s + \gamma S = -\tfrac{4}{3}\pi r^3 \Delta\omega_{ls} + 4\pi r^2 \gamma \tag{26}$$

and

$$\gamma(r) = \frac{(\omega - \omega_l)V}{4\pi r^2} + \frac{\Delta\omega_{ls} r}{3}, \tag{27}$$

where $\Delta\omega_{ls} = \omega_l - \omega_s$ is the difference in the grand potential densities in the liquid and solid phases, which represents the capillary pressure. It can be seen that Eq. (26) defines the grand potential of the formation of a nucleus of radius r. Note that all terms on the right-hand side of Eq. (26) depend on the definition of the dividing surface.

The standard procedure to derive the nucleation barrier and the critical nucleus size is to calculate the derivative from Eq. (26) with respect to r with $\frac{\partial(\omega-\omega_l)}{\partial r} = 0$. It yields

$$\Delta\omega_{ls} = \frac{2\gamma}{r} + \frac{\partial\gamma}{\partial r}. \tag{28}$$

The derivative $\frac{\partial\gamma}{\partial r}$ is taken for a stabilized solid cluster, which is in coexistence with the liquid phase having the constant values of $(\omega - \omega_l)V$ and $\Delta\omega_{ls}$, corresponding to the given values of $\bar{\rho}^i$. The radius r is the distance from the center of a cluster (a nucleus). The function $\gamma(r)$ has a minimum at a radius r^s, which is called the radius of the surface tension [31]. Using the relation (27) and $\frac{\partial\gamma}{\partial r}|_{r=r^s} = 0$, one can get an expression for the radius of the surface tension:

$$r^s = \left(p^s_s \frac{3V}{4\pi}\right)^{1/3} \quad \text{(in 3D)}, \tag{29}$$

where

$$p^s_s = \frac{(\omega - \omega_l)}{(\omega_l - \omega_s)} \tag{30}$$

is the solid phase fraction defined in terms of grand potentials. The corresponding interfacial energy from (28) is defined as

$$\gamma(r^s) = \frac{\Delta\omega_{ls} r^s}{2} \quad \text{(in 3D)}. \tag{31}$$

The relation of the nucleation barrier as a function of the critical radius will have the form

$$\Delta G_n \equiv (\omega - \omega_l)V = \tfrac{2}{3}\pi (r^s)^3 \Delta\omega_{ls} = \tfrac{4}{3}\pi (r^s)^2 \gamma(r^s). \tag{32}$$

To determine the minimum of the interfacial energy for a two-dimensional case, one can rewrite Eqs. (26) and (27) as

$$(\omega - \omega_l)A = -\pi r^2 \Delta\omega_{ls} + 2\pi r\gamma \tag{33}$$

and

$$\gamma(r) = \frac{(\omega - \omega_l)A}{2\pi r} + \frac{\Delta\omega_{ls} r}{2}. \tag{34}$$

Similarly, to derive the nucleation barrier for a two-dimensional case, one can calculate the derivative from Eq. (33) with respect to r by using $\frac{\partial(\omega-\omega_l)}{\partial r} = 0$. The resulting expression for a two-dimensional case can be written as

$$\Delta\omega_{ls} = \frac{\gamma}{r} + \frac{\partial\gamma}{\partial r}. \tag{35}$$

Then, from $\frac{\partial\gamma}{\partial r}|_{r=r^s} = 0$ and (34) follows the relation for the radius of the surface energy

$$r^s = \left(p_s^s \frac{A}{\pi}\right)^{1/2} \quad \text{(in 2D)} \tag{36}$$

and the expression for the minimum interfacial energy

$$\gamma(r^s) = \Delta\omega_{ls} r^s \quad \text{(in 2D)}. \tag{37}$$

It can be seen that, for the radius r^s, the difference in the grand potentials $(\omega - \omega_l)B$ in Eq. (26) has a maximum which corresponds to the nucleation barrier ΔG_n. Substituting (37) into (33), one can get the expression for the nucleation barrier as a function of the critical nucleus radius for a two-dimensional case, i.e.,

$$\Delta G_n = (\omega - \omega_l)A = \pi (r^s)^2 \Delta\omega_{ls} = \pi r^s \gamma(r^s). \tag{38}$$

For the calculation of the minimum interfacial energy (in Sec. V), we use Eq. (34), which can be written as

$$\gamma(r^s) = \frac{\left[\omega - \left(\omega_s p_s^s + \omega_l p_l^s\right)\right]A}{2\pi r^s}. \tag{39}$$

B. Definition of the equimolar interfacial energy

In this subsection, we derive the expression for the equimolar radius r^e based on the concept of equimolar dividing surface. According to the definition, the equimolar surface is a surface where the contribution of the diffusion fields is equal to zero. By multiplying Eq. (24) with μ^i and taking the sum, one can get

$$\sum_i^v \mu^i \bar{\rho}^i = \sum_i^v \mu^i \left(\rho_s^i V_s/V + \rho_l^i V_l/V\right) + \sum_i^v \mu^i \rho_I^i S/V. \tag{40}$$

From this relation, one can obtain the corresponding solid phase fraction defined in terms of the diffusion fields by setting $\rho_I^i = 0$ and using $p_s^e = V_s/V$, i.e.,

$$p_s^e = \frac{\sum_i^v \mu^i \left(\bar{\rho}^i - \rho_l^i\right)}{\sum_i^v \mu^i \left(\rho_s^i - \rho_l^i\right)}. \tag{41}$$

Then, the expression for the equimolar radius can be obtained by using $p_s^e = 4\pi (r^e)^3/(3V)$, i.e.,

$$r^e = \left(p_s^e \frac{3V}{4\pi}\right)^{1/3} \quad \text{(in 3D)}. \tag{42}$$

For a two-dimensional case, the expression for the equimolar radius can be derived as

$$r^e = \left(p_s^e \frac{A}{\pi}\right)^{1/2} \quad \text{(in 2D)}. \tag{43}$$

For the case of equimolar surface, Eq. (34) for the interfacial energy reduces to

$$\gamma(r^e) = \frac{F_I(r^e)A}{2\pi r^e}, \tag{44}$$

where

$$F_I(r^e) = \bar{F} - \left(F_s p_s^e + F_l p_l^e\right) \tag{45}$$

is the excess free energy, which stands for the interface. We use Eq. (44) for the calculation of the equimolar interfacial energy in Sec. V.

Finally, Eq. (33) for the case of the equimolar surface transforms to

$$(\bar{F} - F_l)A = -\pi (r^e)^2 (F_l - F_s) + 2\pi r^e \gamma(r^e), \tag{46}$$

where all terms are positive. It is important to mention here that the quantity $(\bar{F} - F_l)A$ is not the actual nucleation barrier because it is not possible to obtain relations such as Eqs. (37) and (38) for the equimolar dividing surface case.

To illustrate the difference between the minimum interfacial energy and the equimolar interfacial energy, we derived useful relations in terms of r^e and r^s. From Eq. (34) follows

$$\gamma(r^e) = \frac{\Delta\omega_{ls}}{2}\left(r^e + \frac{(\omega - \omega_l)A}{(\omega_l - \omega_s)\pi r^e}\right) = \frac{\Delta\omega_{ls} r^e}{2}(1 + k_{se}), \tag{47}$$

where $k_{se} = (r^s/r^e)^2 = p_s^s/p_s^e$. This relation transforms to the relation (37) if $p_s^s = p_s^e$. Using (47), one can rewrite Eq. (38) for the nucleation barrier as

$$(\omega - \omega_l)A = \pi (r^e)^2 \Delta\omega_{ls} k_{se} = \pi r^e \gamma(r^e) \frac{2k_{se}}{1 + k_{se}}. \tag{48}$$

Furthermore, an additional equation for $\gamma(r^e)$ can be evaluated from Eq. (34) by reducing the part accounts for the diffusion fields, i.e.,

$$\gamma(r^e) = \frac{(F_s - F_l)r^e}{2}\left(\frac{p_s^0}{p_s^e} - 1\right), \tag{49}$$

where

$$p_s^0 = \frac{\bar{F} - F_l}{F_s - F_l} \tag{50}$$

is the solid phase fraction in terms of the free energies.

C. Interfacial energy of a slab configuration

In addition to the interfacial energy for a curved liquid-solid interface, we have also calculated the interfacial energy for a slab crystal with two planar interfaces by using the following expressions:

$$\gamma^{\text{slab}}(r^e) = F_I(r^e)A/(2L) \tag{51}$$

and

$$\gamma^{\text{slab}}(r^s) = \left[\omega - \left(\omega_s p_s^s + \omega_l p_l^s\right)\right]A/(2L) = \frac{(\omega - \omega_l)A}{L}. \tag{52}$$

The above expression shows that the interfacial energy of a slab configuration also depends on the location of the dividing interface.

V. RESULTS AND DISCUSSION

In this section, we present the main simulation results obtained from the simulation scheme described in Sec. III. As an example, a typical solid cluster in equilibrium with the surrounding liquid phase, obtained from simulations

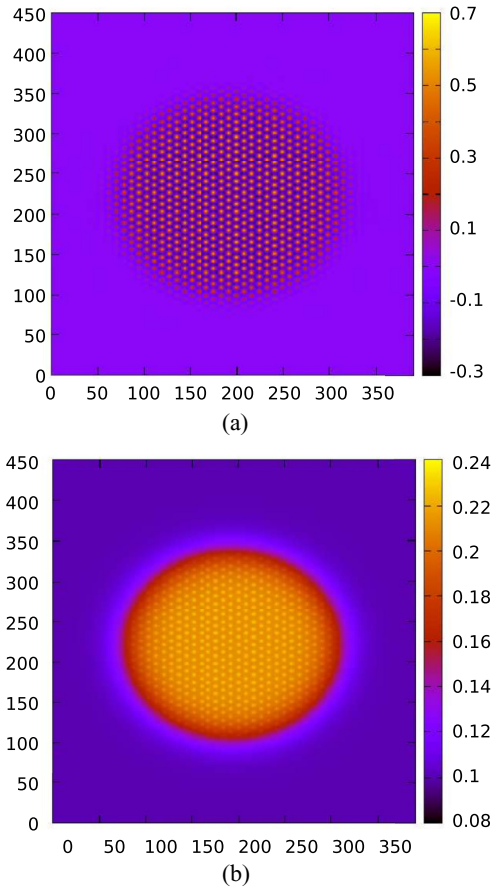

FIG. 3. A stable solid crystal coexists with the surrounding liquid phase for $p_s^{\text{in}} = 0.25$ and $L = 50$: (a) n-diffusion field and (b) c-diffusion field. The x and y axes show the number of grid cells.

performed with $p_s^{\text{in}} = 0.25$ for $L = 50$, is depicted in Fig. 3. The time evolutions the parameters before they arrive the steady state are shown in Fig. 4 for the system size $L = 40$ with $p_s^{\text{in}} = 0.25$. The diffusion potentials μ_s^n and μ_s^c for solid and liquid phases evolve to common mean values, the solid fractions p_s for the equimolar radius and for the minimum radius evolve to steady state values, and the interfacial energies γ for both radii evolve to constant equilibrium values too.

A. Calculation of the equimolar interfacial energy

For the calculation of the equimolar interfacial energy, we use the excess free energy F_I calculated by Eq. (45) as discussed in Sec. IV. The equimolar interfacial energy as a function of the equimolar radius of a solid cluster (r^e) calculated from Eq. (44) is demonstrated in Fig. 5. The equimolar radius is calculated from the solid phase fraction (p_s^e) by using Eq. (43). The values of the interfacial energies obtained for different system sizes follow a master curve which demonstrates that the resulting interfacial energies are independent of the system size.

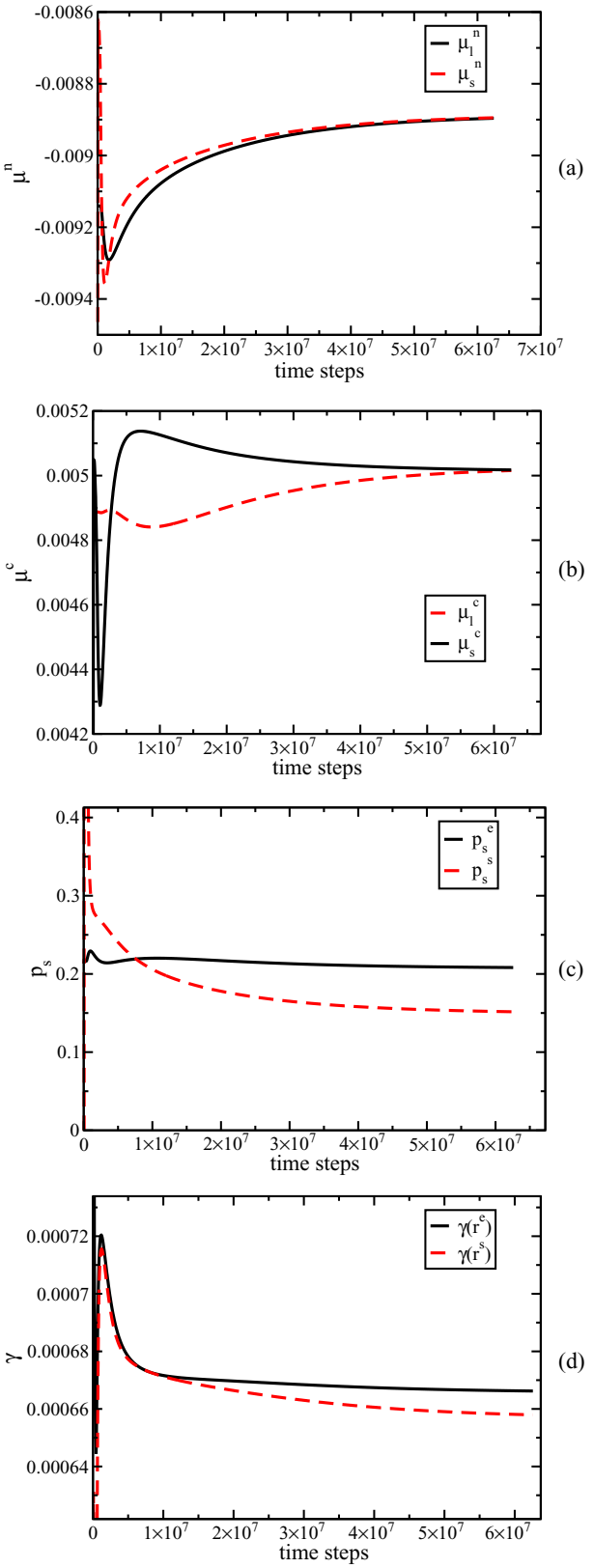

FIG. 4. The time evolution of the diffusion potentials μ_s^n (a), μ_s^c (b), the solid fraction p_s (c), and the interfacial energy γ (d). The system site $L = 40$ and the initial solid fraction is 0.25.

The dependence of the interfacial energy on the cluster radius can be fitted by the following analytical expression

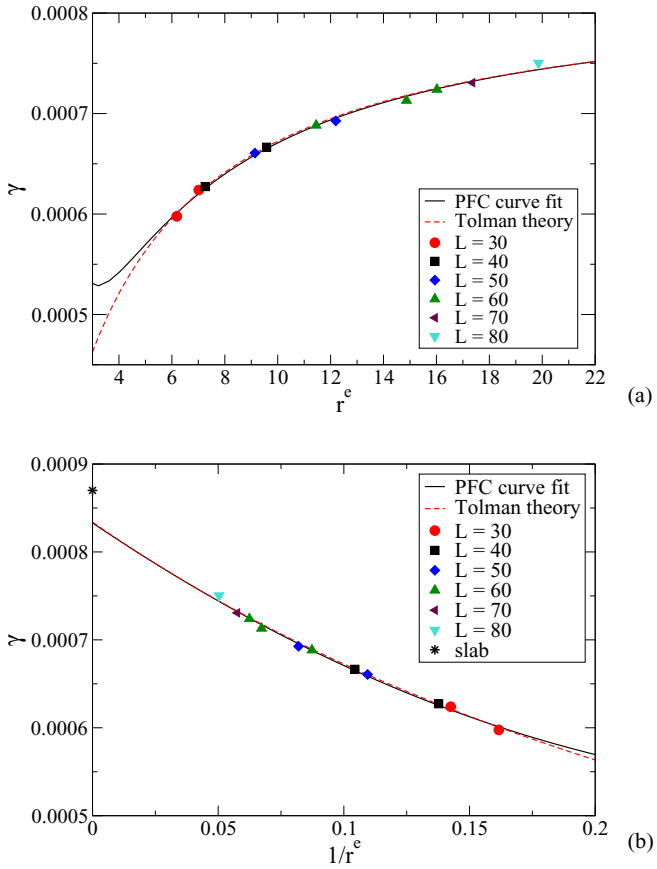

FIG. 5. Dependence of the interfacial energy $\gamma(r^e)$ on the radius r^e for various system sizes as a function of the radius (a) and as a function of the inverse radius (b).

(similar to the expression in Ref. [32] derived from the diffuse interface approach):

$$\gamma(r) = \gamma_\infty\left(1 - \frac{\delta}{r} + a_1\left[\frac{\delta}{r}\right]^2\right), \tag{53}$$

where γ_∞ is the reference interfacial energy, δ is a characteristic length, and a_1 is a numeric constant. The values of these fitting parameters obtained from simulations are listed in Table III. In Fig. 4, the simulation results are also compared with the nonclassical Tolman theory [13]. In this case, the interfacial energy as function of the radius can be described by the formula for 2D case:

$$\gamma(r) = \frac{\gamma_\infty}{\left(1 + \frac{\delta_T}{r}\right)}, \tag{54}$$

where δ_T is the Tolman length. The corresponding fitting parameters are listed in Table III. Both fitting functions give the same correlation coefficient: 0.9975 for equimolar surface and 0.9947 for minimal surface tension. The root mean squared error is equal to 0.0063–0.0066.

TABLE III. The fitting parameters of the dependencies (53) and (54) for the equimolar interfacial energy $\gamma(r^e)$ as well as the minimum interfacial energy $\gamma(r^s)$. For comparison the interfacial energies for the slab configuration γ^{slab} calculated by the PFC model are also listed.

Energy	Function	γ_∞	δ,δ_T	a_1	γ^{slab}
$\gamma(r^e)$	PFC fit Eq. (53)	0.000833	2.313	0.6838	0.000872
$\gamma(r^e)$	Tolman Eq. (54)	0.000834	2.402	0	0.000872
$\gamma(r^s)$	PFC fit Eq. (53)	0.000806	1.678	0.3737	0.000824
$\gamma(r^s)$	Tolman Eq. (54)	0.000825	2.159	0	0.000824

The interfacial energies for the slab were estimated for x and y directions of slab configuration with $L = 50$, $p^{\text{in}} = 0.5$. For r^e we get γ^{slab} (x direction) $= 0.00106$, γ^{slab} (y direction) $= 0.000684$. For r^s we get γ^{slab} (x direction) $= 0.000926$, γ^{slab} (y direction) $= 0.000723$. Then, the average energy of both directions was calculated and used in Table III and Fig. 5. It is important to mention here that the interfacial energies of the slab configuration, calculated from both definitions of dividing surface $\gamma(r^s)$ and $\gamma(r^e)$, go to their limits $\gamma_\infty(r^s)$ and $\gamma_\infty(r^e)$, which are close to each other.

The simulation results in Fig. 5 show that the interfacial energy varies monotonically with r^e and goes to a limit value. It can also be seen that the interfacial energy reaches zero at a critical nucleus radius.

B. Calculation of the minimum interfacial energy

In order to calculate the interfacial energy based on the concept of minimization of interfacial energy, we used Eq. (34). For the calculation of the minimum radius r^s Eqs. (36) and (30) were also used. The resulting interfacial energy as a function of the cluster radius (r^s) is plotted in Fig. 6. It can be seen that the resulting values of the interfacial energies for different system sizes also follows a master curve (similar to Fig. 5). The corresponding fitting parameters for the functions (53) and (54) are listed in Table III. The fitting functions are almost identical.

For the validation of our results, we calculate the values of $\Delta\omega_{ls}r^s$ and the results show that it is equal to the interfacial energy with a precision of up to seven digits in accordance with Eq. (37).

C. Comparison of the dividing surfaces

From the definition of the equimolar surface, it follows that $\mathcal{N}_I \equiv \sum_i \mu^i \rho_I^i$ (the sum of the excess diffusion fields multiplied by the diffusion potentials) is zero for the equimolar surface and nonzero for the other dividing surface concept. Equation (40) transformed to the 2D case was used to calculate $\mathcal{N}_I$ (here the volume quantities should be changed to surface quantities):

$$\mathcal{N}_I = \sum_i^v \mu^i \bar{\rho}^i \frac{A}{2\pi r} - \sum_i^v \mu^i \left(\rho_s^i \frac{\pi r^2}{2\pi r} + \rho_l^i \frac{(B - \pi r^2)}{2\pi r}\right). \tag{55}$$

The dependencies of $\mathcal{N}_I$ on the distance from the center of the cluster are plotted in Fig. 7 for particular choices of $p_s^{\text{in}} = 0.25$ and $L = 40{,}50$. The equimolar radius, which corresponds to $\mathcal{N}_I(r^e) = 0$, and the radius r^s are indicated by dashed lines. Our simulation results demonstrate that the dependence of $\mathcal{N}_I$

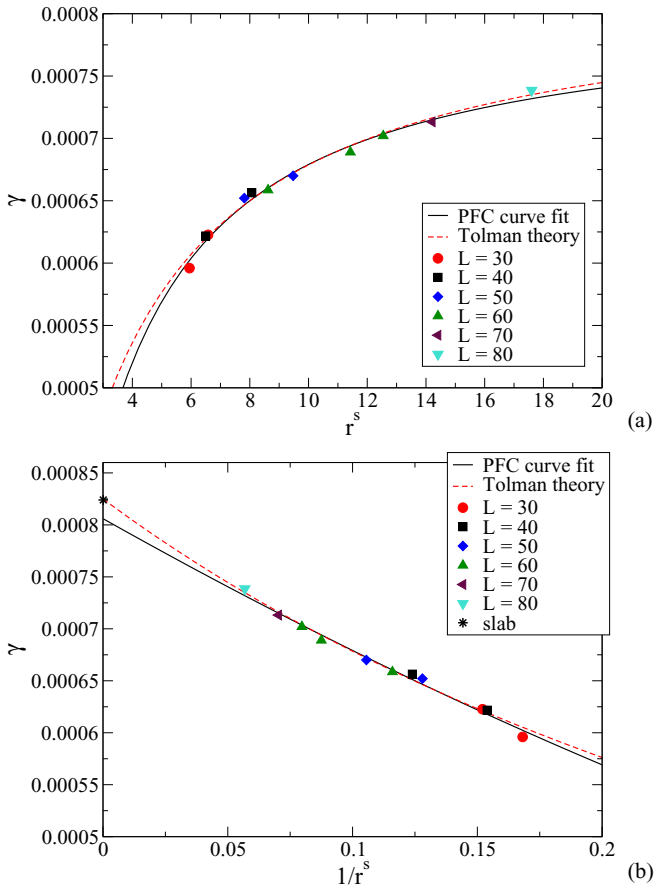

FIG. 6. Dependence of the interfacial energy $\gamma(r^s)$ on the radius r^s for various system sizes as a function of the radius (a) and as a function of the inverse radius (b).

on the radius is similar to the dependence obtained previously from nonclassical investigations of a liquid-vapor system [27]. However, the values of r^e are larger than r^s.

In order to define the dividing surface which has the minimum interfacial energy, we have used parameters from the phase coexistence data and calculate the interfacial energy

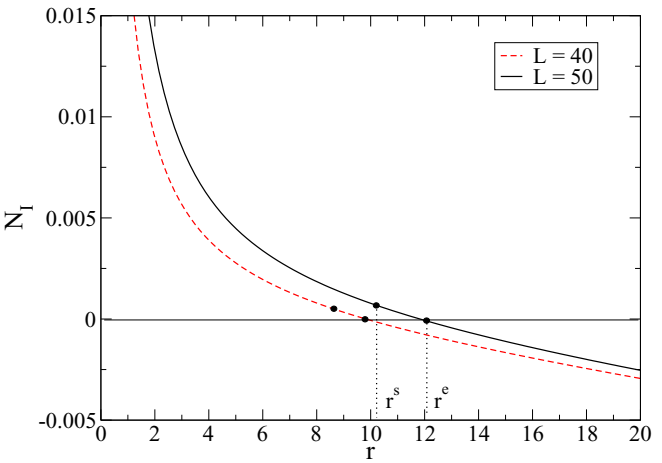

FIG. 7. Dependence of N_I on the distance from the center of the solid cluster for $L = 40$ and $L = 50$ and a particular choice of $p_s^{\text{in}} = 0.25$.

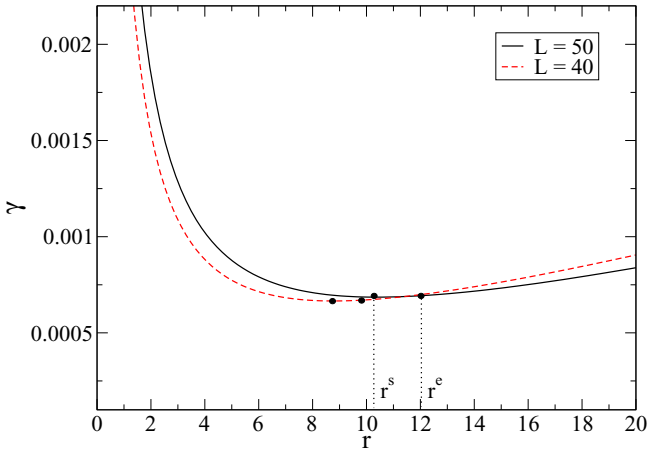

FIG. 8. Dependence of the interfacial energy γ on the distance from the center of the solid cluster for $L = 40$ and $L = 50$ and a particular choice of $p_s^{\text{in}} = 0.25$. The radius corresponding to the minimum interfacial energy and the equimolar radius are indicated.

by using Eq. (34). The resulting dependencies of γ on the distance from the center of a solid cluster are plotted in Fig. 8 for the particular choices of $p_s^{\text{in}} = 0.25$ and $L = 40,50$. The minimum interfacial energy and both radii are indicated by dashed lines. The results show again that the values of r^e are larger than r^s.

The difference between radii, calculated from both definitions of dividing surface, is further demonstrated by plotting $r^e - r^s$ as function of r^e in Fig. 9. The value $r^e - r^s$ for the slab configuration was calculated as $(\sqrt{p_s^e} - \sqrt{p_s^s})\sqrt{A/\pi}$ for the x direction. It can be seen that the radius r^s is smaller than the equimolar radius r^e and the difference between the radii increases with increasing cluster size. In previous investigations of both radii for a liquid droplet [13,27] it was shown that with increasing density field (that corresponds to the increasing droplet radius) the difference $r^e - r^s$ decreases and goes to a limit, which is the Tolman length, and this value is negative, because r^s becomes larger than r^e. Contrary to a liquid droplet in a gas phase, our simulation results for solid-liquid coexistence demonstrate a positive Tolman length, i.e., $r^e > r^s$. The results for the Tolman length are comparable to the calculations in the work of Toth and Granasy [29], where the Tolman lengths were estimated for pure Cu, pure Ag, and for a Cu-Ag alloy as positive values of order 1–4 angstrom (see Fig. 13 in [29]). Hence a positive Tolman length is a common characteristic for the crystal nucleation. In this context, it is worth mentioning that the presence of an additional diffusion field in binary alloys can influence the magnitude of the Tolman length. To investigate the effect of the second component on the Tolman length more precisely, the results of the binary PFC model can be compared to the one-component PFC model in future work.

In Fig. 9, we show the fitting function of inverse radius for the calculated values of the Tolman length $\delta_T = r^e - r^s$:

$$\delta_T = 5.442\left(1 - \frac{6.269}{r^e}\right), \tag{56}$$

where the correlation coefficient is equal to 0.9744 and the root mean squared error is equal to 0.431.

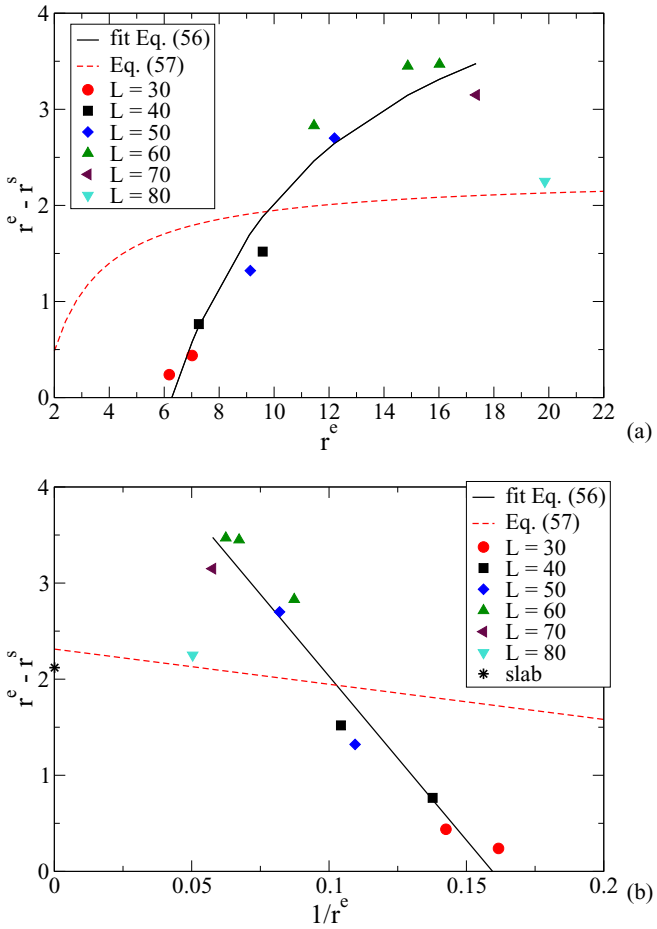

FIG. 9. Difference of radii $r^e - r^s$ for various system sizes as a function of the radius r^e (a) and as a function of the inverse radius $1/r^e$ (b). The solid line is the fitting function.

The Tolman length as a function of the characteristic length and the inverse radius was evaluated from Eq. (53) in the form

$$\delta_T = \delta\left(1 - a_1\frac{\delta}{r^e}\right) \tag{57}$$

with parameters taken from Table III and plotted in Fig. 9 for comparison. Note that for Eq. (54) the Tolman length is a constant. The difference between the calculated values $r^e - r^s$ and the Tolman length defined by the expression (57) can be observed. This difference is too high to be explained by the insufficient precision of the PFC method because it is up to the eighth digit, as shown in our previous work [24] by the comparison with the mode expansion method.

D. Calculation of the nucleation barrier

First, we have calculated the nucleation barrier for our two-dimensional system by using relations given in Sec. IV. The critical nucleus radius r_c can be evaluated from Eq. (33) with $\frac{\partial(\omega-\omega_l)}{\partial r}|_{r_c} = 0$ as $r_c = \frac{\gamma(r_c)}{\Delta\omega_{ls}(r_c)-\partial\gamma/\partial r}$. The standard relation for the nucleation barrier can be obtained if one omits the

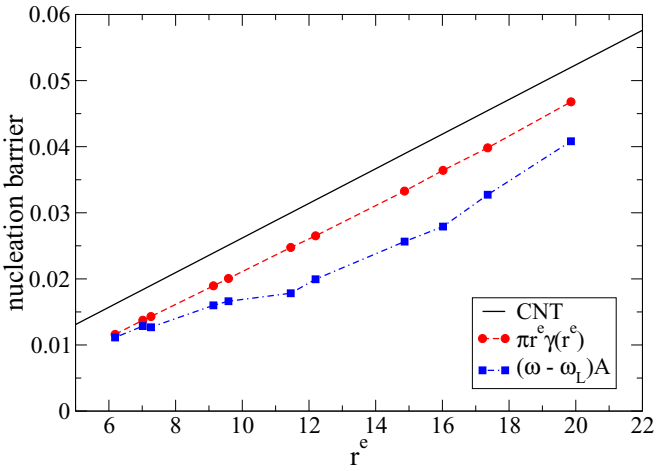

FIG. 10. The real nucleation barrier $\Delta G_n = (\omega - \omega_l)A$ as a function of the equimolar radius calculated from PFC simulation (square symbols and dash-dotted line), the nucleation barrier $\Delta G_n^e = \pi r^e \gamma(r^e)$ (symbols and dashed line), and the classical nucleation barrier $\Delta G_n^{\mathrm{CNT,e}} = \pi r^e \gamma_\infty(r^e)$ (solid line).

dependency of the interfacial energy on the radius, i.e.,

$$\Delta G_n = \pi r_c \gamma(r_c). \tag{58}$$

In order to evaluate the nucleation barriers with the interfacial energy depending on the curvature based on the concept of equimolar dividing surface, we insert the values of the equimolar radius r^e and the corresponding equimolar interfacial energies from our simulation results in Eq. (58). The resulting nucleation barrier $\Delta G_n^e = \pi r^e \gamma(r^e)$ as a function of the equimolar radius is plotted in Fig. 10 as dashed line. This dependency is compared to the classical nucleation theory $\Delta G_n^{\mathrm{CNT,e}} = \pi r^e \gamma_\infty(r^e)$ (solid line), where $\gamma_\infty(r^e)$ is the fitting parameter of Eq. (54) for the equimolar surface (see Table III). The deviation from the CNT can be seen, which occurs due to the curvature dependency of the interfacial energy.

Figure 10 demonstrates (by the dash-dotted line) the dependency of the real nucleation barrier $\Delta G_n = (\omega - \omega_l)A$ on the equimolar radius r^e. The comparison of the dependencies $\pi r^e \gamma(r^e)$ and $(\omega - \omega_l)A$ shows that the value of $(\omega - \omega_l)A$ is much smaller and that it is not possible to calculate precisely the real nucleation barrier as function of the radius by using the equimolar interfacial energy $\gamma(r^e)$. That is in agreement with the theoretical relation (48).

Second, in addition to the nucleation barriers based on the equimolar surfaces, we have also calculated the nucleation barriers based on the concept of minimum interfacial energy with the radius r^s. Figure 11 demonstrates that the dependency of the real nucleation barrier $\Delta G_n = (\omega - \omega_l)A$ and the dependency of the nucleation barrier based on the minimum interfacial energy $\Delta G_n^s = \pi r^s \gamma(r^s)$ on the radius r^s are equivalent. The dependencies are shown as the dashed and dash-dotted lines. The simulation results are in agreement with the nucleation theory [see Eq. (38)]. The comparison to the classical nucleation barrier, $\Delta G_n^{\mathrm{CNT,s}} = \pi r^s \gamma_\infty(r^s)$ (solid line), shows that for small r^s the values of the nucleation barrier $(\omega - \omega_l)A$ differ from the classical theory, again due to the curvature dependence of the interfacial energy. Here

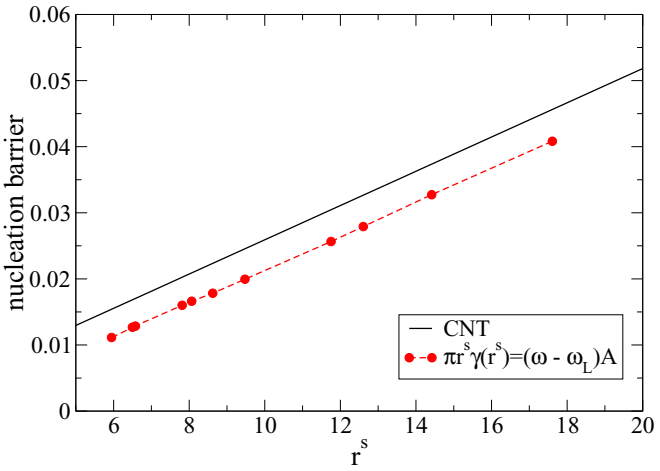

FIG. 11. The real nucleation barrier $\Delta G_n = (\omega - \omega_l)A$ and the nucleation barrier $\Delta G_n^s = \pi r^s \gamma(r^s)$ as a function of the cluster radius r^s obtained from PFC simulation (symbols and dashed line). The solid line indicates the classical nucleation barrier $\pi r^s \gamma_\infty(r^s)$.

$\gamma_\infty(r^s)$ is again the fitting parameter of Eq. (54) for the radius of surface tension.

In summary, the simulation results presented in Figs. 10 and 11 confirm that the nucleation barrier for small nuclei can be evaluated by using the minimum interfacial energy which is defined based on the minimum radius r^s.

VI. CONCLUSION

In this article, we investigated the effect of the dividing surface on the interfacial energy and the nucleation barrier by means of a binary PFC model in two dimensions. For the chosen set of model parameters, a part of the equilibrium phase diagram was calculated, which we used in further numerical investigations. We have employed the method of stabilizing the solid clusters in the liquid matrix in finite systems [24]. To define the dividing surface and the corresponding radius of a cluster, we have used the concept of the equimolar dividing surface and the concept of the minimization of the interfacial energy.

The simulation results show that for both concepts the interfacial energies $\gamma(r^s)$ and $\gamma(r^e)$ increase monotonically with cluster radius and go to their specific limits $\gamma_\infty(r^s)$ and $\gamma_\infty(r^e)$, respectively, which are the interfacial energies for slab configurations. The resulting values of the interfacial energies calculated for various system sizes follow the master curves, and the curvature effect on interfacial energy can be accurately described by a fitting equation which is a little different from the nonclassical Tolman formula. The comparison of simulation results shows that the minimum interfacial energy is smaller than the interfacial energy calculated from the equimolar surface, and the radius of the minimum interfacial energy r^s is smaller than the equimolar radius r^e. Furthermore, the difference $r^e - r^s$ is comparable to the Tolman length δ_T. The resulting difference $r^e - r^s$ is found to be positive for all radii, and this differs from the finding of previous investigations [13,27] for a liquid-vapor system, where r^s can be larger than r^e and the Tolman length can be negative.

Finally, the dependence of the interfacial energy on the cluster radius was used to analyze the dependency of the nucleation barrier on the critical radius. It was justified that the real nucleation barrier can be evaluated only by using the concept of the minimum interfacial energy with the corresponding radius r^s.

ACKNOWLEDGMENT

This work has been supported by the DFG through its priority program SPP 1296 (Project No. Em 68/26-2).

[1] W. D. Myers, Nucl. Phys. A **204**, 465 (1973).
[2] A. Bohr and B. R. Mottelson, *Nuclear Structure, Volume II: Nuclear Deformations* (W. A. Benjamin, New York, 1975).
[3] S. L. Grishick and C. P. Chiu, J. Chem. Phys. **93**, 1273 (1990).
[4] Z. Kožíšek, Cryst. Res. Technol. **26**, 3 (1991).
[5] P. Harrowell and D. W. Oxtoby, J. Chem. Phys. **80**, 1639 (1980).
[6] M. Yussouff, Phys. Rev. B **23**, 5871 (1981).
[7] C. K. Bagdassarian and D. W. Oxtoby, J. Chem. Phys. **100**, 2139 (1994).
[8] L. Granasy, Materials Science Forum **215-216**, 451 (1996).
[9] L. Granasy, T. Pusztai, and E. Hertmann, J. Cryst. Growth **167**, 756 (1996).
[10] L. Granasy, J. Chem. Phys. **104**, 5188 (1996).
[11] L. Granasy and F. Igloi, J. Chem. Phys. **107**, 3634 (1997).
[12] V. M. Fokin and E. D. Zanotto, J. Non-Cryst. Solids **265**, 105 (2000).
[13] A. Tröster, M. Oettel, B. Block, P. Virnau, and K. Binder, J. Chem. Phys. **136**, 064709 (2012).
[14] H. Furukawa and K. Binder, Phys. Rev. A **26**, 556 (1982).
[15] M. Schrader, P. Virnau, and K. Binder, Phys. Rev. E **79**, 061104 (2009).
[16] K. R. Elder, M. Katakowski, M. Haataja, and M. Grant, Phys. Rev. Lett. **88**, 245701 (2002).
[17] K. R. Elder, N. Provatas, J. Berry, P. Stefanovic, and M. Grant, Phys. Rev. B **75**, 064107 (2007).
[18] P. M. Stefanovic, M. Haataja, and N. Provatas, Phys. Rev. Lett. **96**, 225504 (2006).
[19] J. Berry, M. Grant, and K. R. Elder, Phys. Rev. E **73**, 031609 (2006).
[20] M. A. Choudhary, D. Li, H. Emmerich, and H. Löwen, J. Phys.: Condens. Matter **23**, 265005 (2011).
[21] M. A. Choudhary, J. Kundin, and H. Emmerich, Philos. Mag. Lett. Matter **92**, 451 (2012).
[22] M. A. Choudhary, J. Kundin, and H. Emmerich, Comput. Mater. Sci. **83**, 481 (2014).
[23] J. Kundin, M. A. Choudhary, and H. Emmerich, Eur. Phys. J. Spec. Top. **223**, 363 (2014).
[24] M. A. Choudhary, J. Kundin, H. Emmerich, and M. Oettel, Phys. Rev. E **90**, 022403 (2014).

[25] J. W. Gibbs, *Collected Works, Volume I* (Longmans Green and Company, New York, 1982).
[26] R. C. Tolman, J. Chem. Phys. **17**, 333 (1949).
[27] V. M. Kolomietz, S. V. Lukyanov, and A. I. Sanzhur, Phys. Rev. C **86**, 024304 (2012).
[28] V. M. Kolomietz and A. I. Sanzhur, Phys. Rev. C **88**, 044316 (2013).
[29] G. I. Toth and L. Granasy, J. Chem. Phys. **127**, 074709 (2007).
[30] J. Kundin, R. Schmid-Fetzer, P. Wang, and H. Emmerich, Eur. Phys. J. Spec. Top. **223**, 567 (2014).
[31] J. S. Rowlinson and B. Widom, *Molecular Theory of Capillarity* (Clarendon Press, Oxford, 1982).
[32] H. Assadi and J. Schröders, Acta Mater. **50**, 89 (2002).